Optical spectroscopy and four-wave mixing in emerald

Gregory J. Quarles,* Andrzej Suchocki,† and Richard C. Powell
Department of Physics, Oklahoma State University, Stillwater, Oklahoma 74078-0444

Shui Lai
Allied Signal, Inc., Morristown, New Jersey 07960

(Received 21 December 1987; revised manuscript received 2 May 1988)

The optical-spectroscopic properties of Cr^{3+} ions in $Be_3Al_2(SiO_3)_6$ crystals were investigated using several techniques. The temperature dependencies of the fluorescence intensity and lifetime were measured between 10 and 300 K and shown to be due to thermal population effects in the $^4T_2$ and ^2E levels. The results of time-resolved site-selection spectroscopy measurements show that the Cr^{3+} ions occupy several different types of sites having nonequivalent crystal fields, and that spectral energy transfer takes place between ions in different types of sites. The results of four-wave mixing measurements show the presence of long-range resonant energy migration among the chromium ions and provide information about the radiationless relaxation rate from the $^4T_2$ level to the ^2E level.

I. INTRODUCTION

The potential use of emerald [$Be_3Al_2(SiO_3)_6:Cr^{3+}$] as a tunable solid-state laser material[1–3] has generated renewed interest in understanding the details of the spectroscopic properties of this crystal. Although the general optical spectroscopic properties of emerald have been characterized,[4–9] there are still important unanswered questions concerning the local crystal-field environment of the Cr^{3+} ions, the characteristics of energy transfer among the Cr^{3+} ions, and the details of radiationless transition in this material. We report here the results of investigating the optical properties of emerald using several different spectroscopic techniques, including time-resolved site-selection spectroscopy (TRSSS) and four-wave mixing (FWM). The results show that the Cr^{3+} ions occupy sites having several different types of local crystal-field environments and that this leads to two different types of energy-transfer processes in this material. The first is a short-range process between ions in sites having nonequivalent crystal-field environments, while the second is a resonant, long-range migration process. These processes are characterized in terms of Frenkel excitons with the mobile excitation energy localized on a Cr^{3+} ion. The radiationless transitions distributing the population of excited ions among the $^4T_2$ and ^2E levels are shown to be responsible for the temperature dependences of the fluorescence intensity and lifetime and for the dephasing time of the four-wave mixing signal.

The sample was used in this work had a rectangular shape of dimensions $7.5\times13\times3.8$ mm and a dark-green color. It was grown by the hydrothermal method and contained 3 at. % Cr^{3+} ions ($N_0=1.77\times10^{20}$ cm^{-3}). Emerald has the beryl structure with a space group designated as $P6/mcc$ and two molecules per unit cell.[10] The Cr^{3+} ions substitute for the Al^{3+} ions and "sit" at the center of a slightly distorted octahedral site, as is seen in Fig. 1. The site symmetry of Cr^{3+} in this lattice is[11,12] D_3. The dominant structure in beryl is the Si_6O_{18} rings which are linked by Be and Al ions. As noted on Fig. 1, the first- and second-nearest-neighbor distances for the Cr^{3+} sites are 4.6 and 5.3 Å, respectively.[10] This is much larger than the 2.65- or 2.7-Å first-nearest-neighbor distances found in similar Cr^{3+}-doped laser materials, ruby[13] and alexandrite,[14] respectively. These larger distances between Cr^{3+} ions allow for high concentrations without appreciable concentration quenching of the fluorescence. However, the tradeoff is that the density of available sites for Cr^{3+} in beryl is 5.9×10^{21} cm^{-3}, which is approximately 12% of that in the corundum lattice of ruby.[9] For emerald doped with 3 at. % Cr^{3+} there is evidence for the presence of exchange coupled pairs of Cr^{3+}

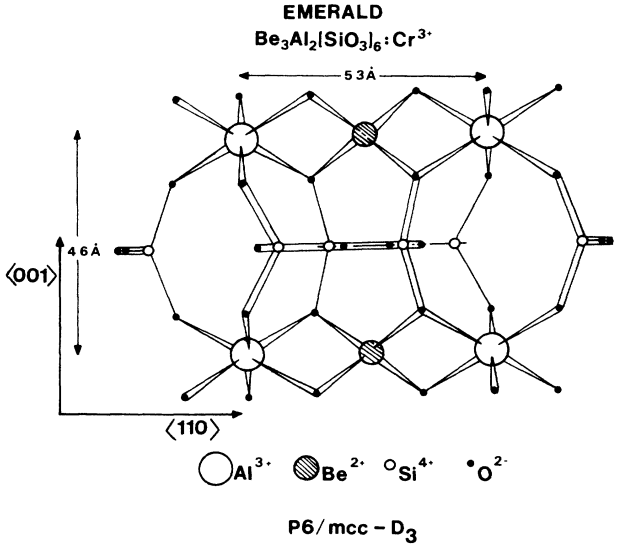

FIG. 1. Crystal structure of beryl projected onto a (100) plane. (Taken from Ref. 9.)

ions.[10] Also, at this high level of concentration there is a considerable amount of internal strain in the crystal, causing different local crystal-field environments for the Cr^{3+} ions which results in inhomogeneous broadening of the optical transitions. Both the exchange coupling and microscopic strains can contribute to the spectral structure described in Sec. II.

II. OPTICAL SPECTROSCOPIC PROPERTIES

The absorption and fluorescence spectra of emerald at 70 K are shown in Figs. 2 and 3. The former was obtained using an IBM 9430 UV-Visible Spectrophotometer. The latter was taken using the 488-nm line of an argon laser for the excitation, a 1-m Spex monochromator for spectral dispersion, a RCA-C31034 photomultiplier tube to detect the signal, and a lock-in amplifier to enhance the signal-to-noise ratio. The sample was placed in a cryogenic refrigerator in order to control the temperature. Front-surface excitation of the fluorescence was used to minimize the effects of reabsorption. The peaks in the absorption spectrum are labeled in terms of the octahedral crystal-field designations of the final states of their transitions from the $^4A_2$ ground state. The fluorescence is associated with zero-phonon transitions from the crystal-field-split components of the ^2E level (R lines) and broadband fluorescence, which is a superposition of the vibronic sideband of the R lines and emission from the $^4T_2$ level.

Figure 4 shows the absorption and fluorescence spectra in the region of the R lines at 70 K uncorrected for polarization effects. (The effects of polarization on the spectra are clearly shown in Ref. 3.) Both fluorescence and absorption spectra were taken at temperatures ranging from 10 to 300 K, but the structure in the R_1 and R_2 lines becomes most visible around 70 K. These lines are inhomogeneously broadened with large linewidths, consistent with results reported previously.[15] The fluorescence spectra were obtained with cw excitation at 457.9 nm. Both of the R lines in fluorescence exhibit a structure

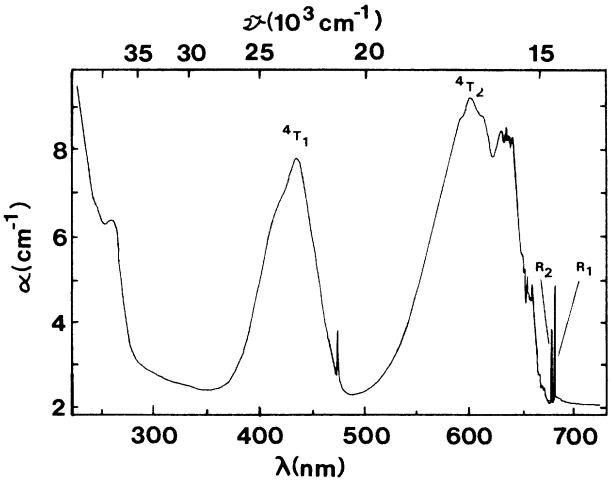

FIG. 2. Absorption spectrum of emerald with 3 at. % Cr^{3+} at $T=70$ K.

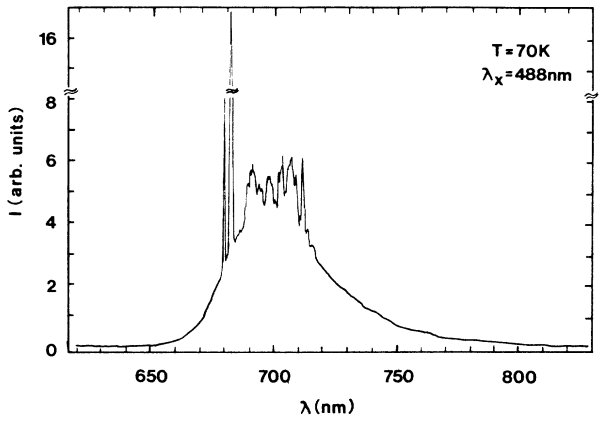

FIG. 3. Fluorescence spectrum of emerald with 3 at. % Cr^{3+} at $T=70$ K using 488-nm excitation from an argon-ion laser.

consisting of four peaks, and some structure is also observed in absorption. The positions of these components are listed in Table I. Each peak is designated with superscripts, but it is not clear how the peaks in R_1 correlate with those in R_2. Assuming that each of the peaks is associated with a different local crystal-field environment for the Cr^{3+} ion, and assuming the same oscillator strength for the $^4A_{2g} \rightarrow {}^2E_g$ transition for each type of environment, it is possible to estimate the relative concentrations of the Cr^{3+} ions in each of the different environments from the absorption spectra of the R lines. These values are listed in Table I.

The decay kinetics of the fluorescence excitating at 588 nm were monitored using a boxcar integrator. The sig-

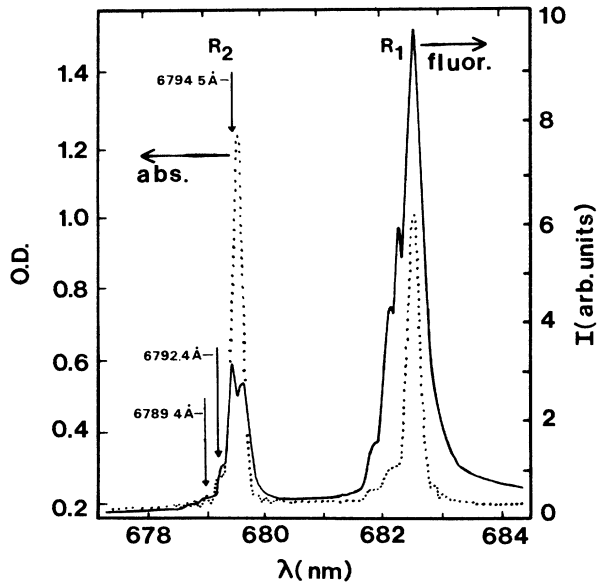

FIG. 4. High-resolution fluorescence and absorption spectra of the R lines in emerald at 70 K. The vertical arrows indicate excitation wavelengths used in site-selection spectroscopy. O.D. is the optical density.

TABLE I. Spectral properties of the R lines of emerald with 3 at. % Cr^{3+} at 20 K.

Parameter	Site a	b	c	d	e
Peak position λ_{R_1} (nm)					
Absorption	681.55	681.80	682.25		682.60
Fluorescence		681.80	682.20	682.30	682.60
Peak position λ_{R_2} (nm)					
Absorption	678.80	678.95	679.24	679.56	
Fluorescence		678.95	679.25	679.50	679.65
Concentration of ions					
N_t ($\times 10^{18}$ cm^{-3})	1.72	3.68		171.60[a]	
Fluorescence decay time τ (ms)					
$\lambda_{ex}=678.94$ nm		1.112			1.436
		0.317			
$\lambda_{ex}=679.24$ nm		1.859	1.079		1.610
		0.707	0.351		
$\lambda_{ex}=679.45$ nm			1.540		1.575
Fluorescence rise time t_r (μs)					
$\lambda_{ex}=678.94$ nm		83.89			218.7
$\lambda_{ex}=679.24$ nm		95.86	112.0		213.2
$\lambda_{ex}=679.45$ nm			149.8		364.2

[a]This represents the sum of the concentrations of ions in sites c and d since their transitions are not well resolved; the transition from ions in site e is too small to determine an accurate concentration.

nals were found to be single-exponential decays over two decades between 12 and 200 K. The decay time of the fluorescence was 1.7 ms at temperatures below 60 K. This is slightly longer than the low-temperature lifetimes reported by Kisliuk and Moore[16] and by Hassan *et al.*[9] In both of these cases it was suggested that traces of Fe^{2+} ions quenched the Cr^{3+} fluorescence. Above 60 K the lifetime decreases with increasing temperature due to thermal population of the $^4T_2$ level. The temperature dependence of the fluorescence lifetime is shown in Fig. 5. A theoretical prediction for the temperature dependence of the fluorescence lifetime can be obtained from the expression

$$\tau^{-1}=\tau_E^{-1}+\tau_T^{-1}\exp(-\Delta E/k_BT) . \quad (1)$$

Here it has been assumed that the ^2E and $^4T_2$ levels are separated by an energy ΔE and their populations are in thermal equilibrium. τ_E and τ_T are the intrinsic lifetimes of these levels and it is assumed that the intermediate $^2T_1$

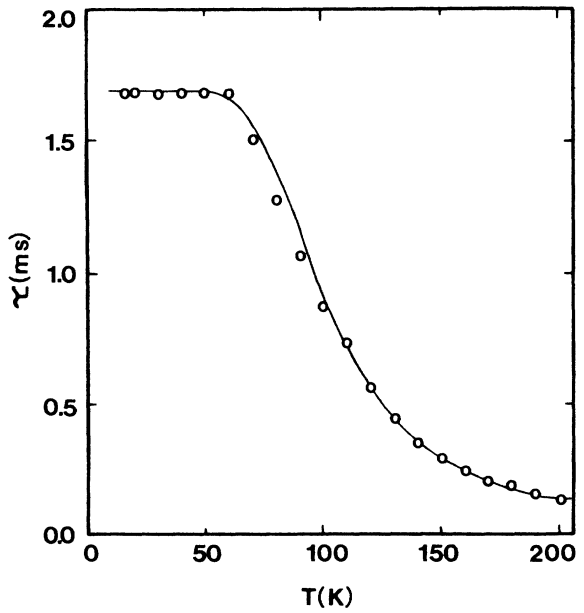

FIG. 5. Temperature dependence of the fluorescence lifetime of emerald.

TABLE II. Spectral energy transfer parameters for emerald with 3 at. % Cr^{3+} at 20 K.

From fitting the temperature dependence of the fluorescence lifetime	
ΔE	381 cm^{-1}
τ_T	14 μs
τ_E	1.7 ms
From time-resolved site-selection spectroscopy results	
$I_a(0)/I_s(0)$	0.085
Ω	15.59 $s^{-1/2}$
R_0	7.42 Å
From fitting the fluorescence-decay kinetics	
α''	4.67×10^{-41} cm^6/s
D_n	6.51×10^{-13} cm^2/s
a'	15.98 Å
R_0	6.11 Å
Theoretical prediction	
D_n	4.6×10^{-13} cm^2/s

levels do not play a significant role in the spectral dynamics.[16] Using Eq. (1) with the intrinsic lifetimes and the energy gap treated as adjustable parameters, the best fit to the data is shown as a solid line in Fig. 5. The value of the energy gap between the ^2E and the $^4T_2$ levels is found to be equal to 381 cm^{-1}, which is in good agreement with previous reported values.[16,17] The intrinsic decay time of the $^4T_2$ level was found to be 14 μs, which is close to the values found from previous investigations.[9,16] The intrinsic lifetime of the ^2E level was found to be 1.7 ms. The parameters used in obtaining this fit are listed in Table II.

III. TIME-RESOLVED SITE-SELECTION SPECTROSCOPY

Time-resolved site-selection spectroscopy (TRSSS) measurements were used to characterize the properties of short-range spectral energy transfer between Cr^{3+} ions with different crystal-field environments in emerald. A nitrogen-laser-pumped dye laser, using Oxazine 720 dye with a narrow linewidth (<0.6 Å) was used to selectively excite the Cr^{3+} ions having a specific type of crystal-field environment. Excitation in the R_2 line typically yields three emission peaks in the R_1 line, and the energy transfer is predominantly from ions in crystal-field environments, resulting in higher-energy transitions to those in environments having lower-energy transitions. Using the labeling scheme from Table I, the ions with environments giving transitions *a* and *b* act as sensitizers and those with the environment giving transition *d* act as activators. It was not possible to resolve the *c* or *e* transitions using nanosecond pulse excitation into the R_2 line, and thus ions with environments giving rise to these transitions are also counted as activators. By taking spectral scans of the fluorescence emission at different times after the laser-excitation pulse, it was possible to characterize the time evolution of the energy transfer between Cr^{3+} ions having different crystal-field environments.

The experimental apparatus for the TRSSS measurements has been described previously.[18] The emerald sample was excited using three different laser wavelengths, 6789.4, 6792.4, and 6794.5 Å, which are shown as vertical arrows in the R_2 absorption line in Fig. 4. The fluorescence spectra of the R_1 lines were then spectrally resolved through a 1-m monochromator and directed onto a RCA-C31034 photomultiplier tube. The input and output slits were maintained at 100 μm to ensure a resolution of ≤ 0.4 Å.

Figure 6 shows the typical fluorescence spectrum of the R_1 lines at 20 K and at 1.00 ms after excitation at 6789.4 Å. It was possible to resolve three separate peaks in the fluorescence as shown in the figure. To study the spectral energy transfer, it is necessary to know the area associated with each peak and how it evolves with time. To get a good estimate for the area, the data were deconvoluted with a curve-fitting routine that fitted three overlapping Gaussian peaks to the fluorescence spectra. The separate Gaussians are denoted by the dashed lines in Fig. 6, with the overall fit shown by the solid line. The Gaussian profile fits the data quite well. From the curve-fitting routine it was possible to obtain the total area, the peak

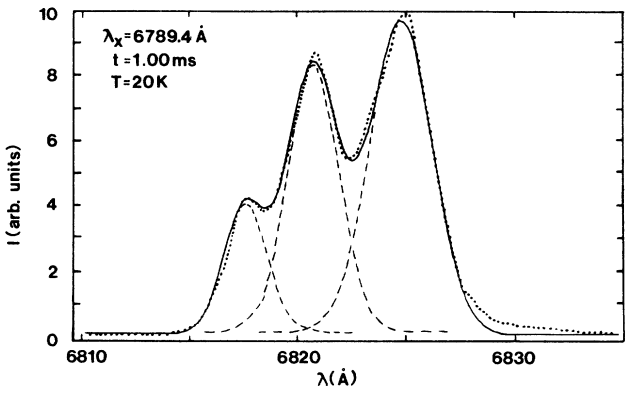

FIG. 6. Fluorescence spectra of the R_1 lines in emerald at 1.0 ms after the pulse after selectively exciting the R_2 line at 6789.4 Å at 20 K. The dots represent experimental data points and the dashed and solid lines represent the fitting with three overlapping Gaussian curves.

wavelength and intensity, and the full width at half maximum for each Gaussian component.

The fluorescence risetimes and lifetimes of each of the three peaks were monitored for each excitation wavelength and temperature, and their values at 20 K are listed in Table I. The two highest-energy peaks are both double-exponential decays with fast risetimes, while the lowest-energy peak is single exponential over two decades with a much longer risetime. The accuracy of the lifetimes and risetimes is approximately $\pm 5\%$. To characterize the properties of energy transfer between ions with different types of crystal-field environments, the two highest-energy peaks are designated as being from sensitizer ions and the lowest-energy peak as being from activator ions, as discussed above. Figure 7 shows the fluorescence spectra of the R_1 lines for four different temperatures at 100 μs after the three different excitation wavelengths. As the excitation wavelength is shifted to lower energy, the number of distinct peaks decreases until there is only one fluorescence peak remaining, that being associated with the emission from the activator ions excited by the lowest-energy excitation wavelength. There is also very slight backtransfer from activator to sensitizer sites, noticeable mostly at higher temperatures. Figure 8 shows the fluorescence spectra at 20 K, for the three excitation wavelengths, at five different times after the pulse. The two highest-energy peaks (transitions from sites *a* and *b*) evolve at approximately the same rate, while the lowest-energy peak (transitions from sites *c*, *d*, and *e*) evolves more slowly and becomes the dominant peak at the longer times after the pulse.

The time evolution of the R_1 lines is demonstrated in Fig. 9, which shows the changes in the ratios of the integrated fluorescence intensities of the activator transition to that of the sensitizer transition. These areas are taken from the fits of the experimental data with Gaussian curves. There is an initial buildup of the ratios of the relative area of the transitions and, at longer times after

the pulse, an equilibrium condition is approached.

The time evolution of the ratios can be modeled using a phenomenological rate-parameter model.[18] The sensitizer ions are those preferentially excited by the laser at a rate W_s, whereas the activator ions receive the energy through energy transfer as well as a small amount of direct pumping at a rate W_a. n_a and n_s are the concentrations of the ions in the excited states, W_{sa} is the rate of energy transfer from sensitizer to activator, and β_a and β_s are the fluorescence decay rates associated with each type of ion. As noted above, the time-resolved spectral data show that backtransfer from activator ions to sensitizer ions is negligible at low temperatures and weak at high temperatures. Therefore this process is neglected in the analysis. The reason that there is no strong backtransfer in this case is that the concentration of ions in activator sites is much higher than the concentration of ions in sensitizer sites and strong energy transfer occurs among activator ions. This is discussed in detail in the next section. With these assumptions, the rate equations

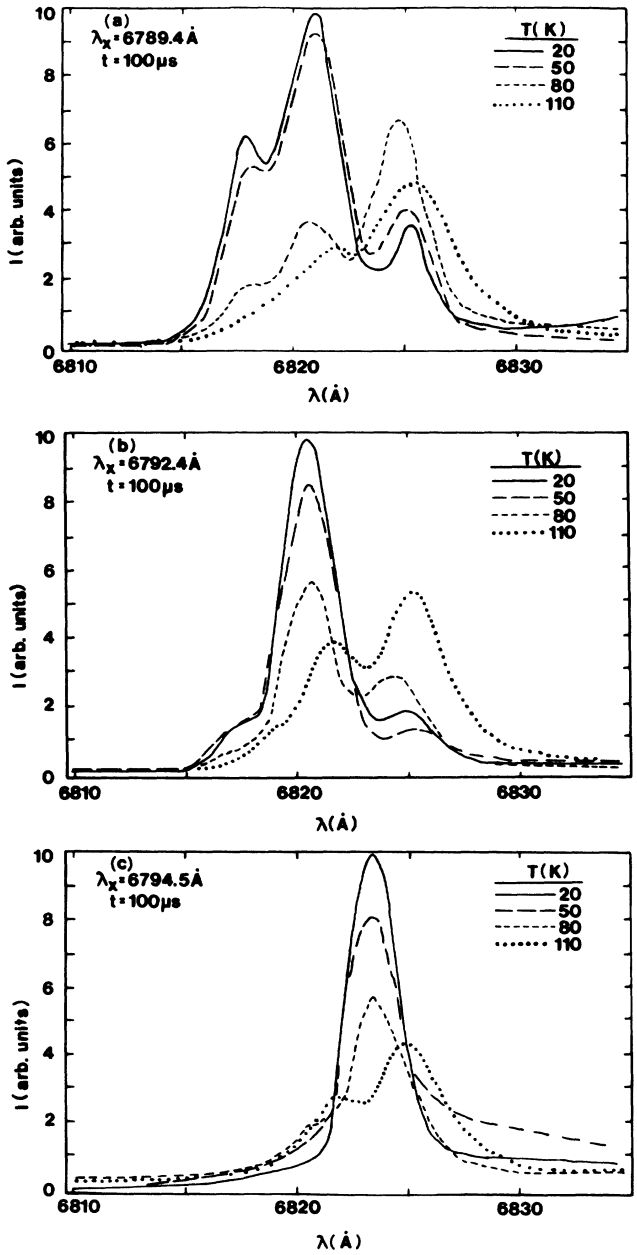

FIG. 7. Fluorescence spectra of the R_1 lines in emerald for different temperatures at 100 μs after the pulse after selectively exciting the R_2 line at (a) 6789.4 Å, (b) 6792.4 Å, and (c) 6794.5 Å.

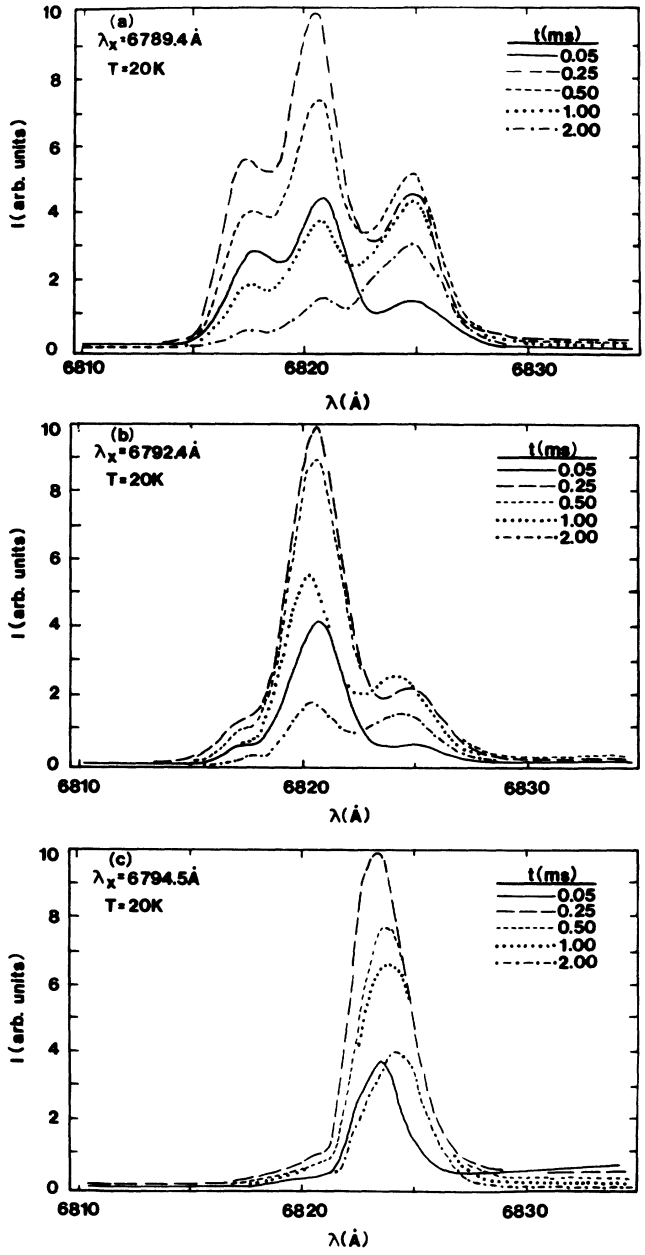

FIG. 8. Fluorescence spectra of the R_1 lines in emerald at 20 K at five different times after the pulse after selectively exciting the R_2 lines at (a) 6789.4 Å, (b) 6792.4 Å, and (c) 6794.5 Å.

describing the time evolution of the populations of the excited state are

$$\frac{dn_s}{dt} = W_s - \beta_s n_s - W_{sa} n_s \ , \tag{2}$$

$$\frac{dn_a}{dt} = W_a - \beta_s n_a + W_{sa} n_s \ . \tag{3}$$

These equations can be solved assuming a δ-function excitation pulse and an explicit time dependence for the energy-transfer rate. The solutions were obtained using various types of time dependencies for W_{sa} associated with different types of energy-transfer mechanisms. It was found that the best fit to the data was obtained with a time dependence for the energy-transfer rate of $t^{-1/2}$. The physical meaning of this time dependence is discussed below. The solutions of Eqs. (2) and (3) in this case are given by

$$n_s(t) = n_s(0)\exp(-\beta_s t - 2\Omega t^{1/2}) \ , \tag{4}$$

$$n_a(t) = n_s(0)[\exp(-\beta_s t) - \exp(-\beta_s t - 2\Omega t^{1/2})] + n_a(0)\exp(-\beta_a t) \ , \tag{5}$$

where the time dependence of the energy-transfer rate is written explicitly as $W_{sa} = \Omega t^{-1/2}$. The ratio of the integrated fluorescence intensities is proportional to the ratios of the excited-state populations,

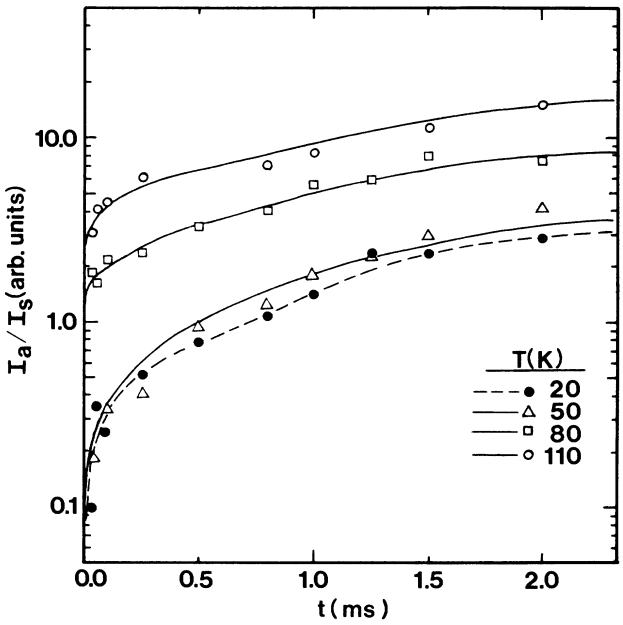

FIG. 9. Time dependence of the ratios of the integrated fluorescence intensities of the R_1 lines from Cr^{3+} ions in sensitizer and activator sites for four different temperatures. The solid and dashed lines represent the theoretical fits to the experimental data using a rate-equation model.

$$I_a/I_s = (\beta_a^r/\beta_s^r)(\{[I_a(0)h\nu_s/I_s(0)h\nu_a](\beta_s^r/\beta_a^r)+1\}\exp(2\Omega t^{1/2})-1) \ , \tag{6}$$

where β_a^r and β_s^r are the radiative decay rates associated with the activator and sensitizer ions, respectively. The solid and dashed lines in Fig. 9 represent the best fits of Eq. (6) to the experimental data, treating $I_a(0)/I_s(0)$ and Ω as adjustable parameters. The values for these parameters at 20 K are listed in Table II.

The $t^{-1/2}$ variation of the energy-transfer rate is characteristic of a single-step electric-dipole–dipole interaction between randomly distributed sensitizers and activators. This time dependence may still be observed when additional energy migration among the sensitizer ions is present. In order to determine the importance of sensitizer energy migration compared to single-step transfer, the change in the fluorescence intensity was monitored as a function of time. This decay can be fitted with an expression for the time evolution of the fluorescence with the energy-transfer rate expressed by an appropriate energy-transfer theory. In each of these theories the excitation energy is treated as a mobile Frenkel exciton localized on a specific ion and able to migrate on a lattice of sensitizer ions. Analysis of the data was attempted using several models and it was found that the best analytical model for describing the transfer kinetics in emerald is that of Chow and Powell.[19] This theory assumes that an exciton is created on the sensitizer site and migrates among the sensitizers, and at each step in the random walk the exciton has a possibility of transferring its energy to any activator in the lattice. It is also assumed for this model that the ion-ion interaction is of electric-dipole–dipole type and that the sensitizer-sensitizer interaction is large compared to that of the sensitizer-activator interaction. Thus, the energy-transfer rate is given by[19]

$$W_{sa} = 4\pi N_a D_n a'[1 + a'(\pi D_n t)^{-1/2}] + 4\pi N_a \alpha''/3a'^3 + 2\pi N_a a'^2 \int_{a'}^{\infty} dr\,(\alpha''/r^6)\{\mathrm{erfc}[(r-a')/(4D_n t)^{1/2}]\}^2 - 8\pi N_a a' \int_{a'}^{\infty} dr\,(\alpha''/r^5)\{\mathrm{erfc}[(r-a')/(4D_n t)^{1/2}]\} \ , \tag{7}$$

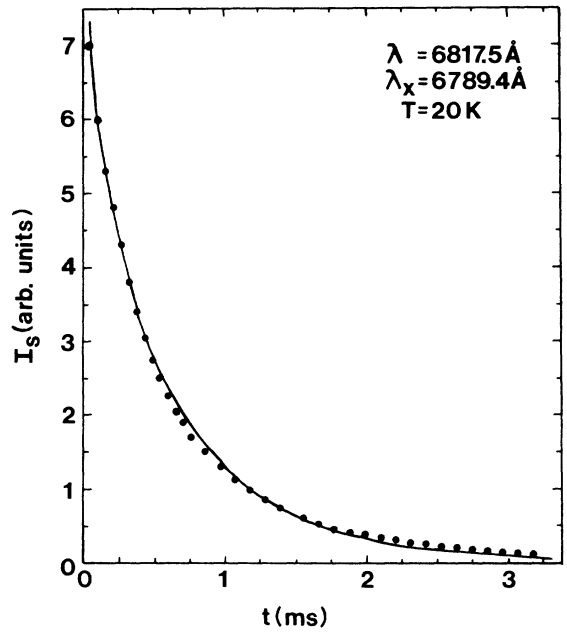

FIG. 10. Time dependence of the fluorescence emission intensity of one sensitizer site of Cr^{3+} in emerald at 20 K. The solid line represents the theoretical fit to the data using the Chow-Powell model for energy transfer.

where N_a is the total number of activators (1.716×10^{20} cm^{-3} as listed in Table I), $\alpha''=R_0^6\beta_s$ is the parameter describing the single-step transfer between a sensitizer and an activator defined in terms of the critical interaction distance R_0 and the sensitizer intrinsic decay rate β_s, D_n is the diffusion coefficient for the random walk among the sensitizer ions, and a' is the trapping radius of an activator ion.

Figure 10 shows the typical results of fitting this equation to one of the experimental decay curves. The agreement between theory and experiment is excellent. The validity of this theory is determined by the criterion that $\pi D_n a'^4 \alpha''^{-1} > 1$. For 20 K the values obtained from the fitting procedure are $D_n=6.51\times10^{-13}$ cm^2/s, $a'=15$ Å, and $\alpha''=4.66\times10^{-41}$ cm^6/s, and these give a typical value of 22.1 for the validity inequality. Thus the criterion is met and we assume that this model accurately describes the spectral energy transfer in emerald. This is in good agreement with the results of previous studies that predicted a dipole-dipole–interaction mechanism for emerald from the analysis of fluorescence-line-narrowing results.[9] Using the analysis of the data described above, the values of D_n were determined at several temperatures and found to be essentially independent of temperature below 100 K. Above this temperature it was difficult to obtain an accurate analysis of the data because of thermal line broadening.

IV. FOUR-WAVE MIXING RESULTS

Four-wave mixing (FWM) measurements were used to characterize the properties of long-range spatial energy migration in emerald. The details of the experimental setup used in this work were described previously in Ref. 20. Crossed laser beams from a ring dye laser were tuned to 588 nm, in order to resonantly pump the $^4T_2$ band. This establishes a population grating of excited Cr^{3+} ions in the sample. The total laser power used in this work was about 300 mW. A He-Ne laser was used as the probe beam and the signal beam was processed by a Princeton Applied Research–EG&G signal averager. By chopping the write beams on and off, the kinetics of the laser-induced grating could be monitored. These are influenced by the fluorescence decay and the spatial migration of Cr^{3+} excitation energy from the peak-to-valley regions of the grating. The primary measurements involved in this work are the variations of the FWM signal efficiency and decay rate with the crossing angle of the write beams. The former provides information about radiationless decay and excited-state–absorption processes, while the latter provides information about the properties of energy migration among the Cr^{3+} ions. Characterizing the energy migration is the main focus of this work.

For a simple sine-wave grating, the scattering efficiency at the Bragg angle is given by[21]

$$\eta=\exp(-2\alpha L)[\sin^2(d\pi\Delta n/2\lambda)+\sinh^2(d\,\Delta\alpha/4)]\ , \tag{8}$$

where α and L are the absorption coefficient and thickness of the sample, and d is the thickness of the grating. Making the assumption that there is little or no beam depletion, and that the product of the grating thickness and the modulation depth is small, Eq. (8) simplifies to

$$\eta\approx(\pi/2\lambda)^2(d^2\Delta n^2)+(\tfrac{1}{4})^2(d^2\Delta\alpha^2)\ . \tag{9}$$

For the type of population grating of interest here, it is possible to estimate the value of $\Delta\alpha$ from the a standard rate-equation analysis of the populations of the energy levels and the transitions between them,[22,23]

$$\Delta\alpha=N_0I_0\sigma_1(\sigma_1-\sigma_2)/(2I_0\sigma_1+h\nu/\tau)\ , \tag{10}$$

where N_0 is the concentration of active ions, I_0 is the intensity of the write beams, τ is the fluorescence lifetime, and σ_1 and σ_2 are the ground- and excited-state absorption cross sections, respectively. A similar expression can be derived for the change in Δn using an oscillator model for the transitions.[23] However, the results involve a sum over oscillator strengths for all possible transitions and this is difficult to calculate accurately.

One method for determining the contributions to the FWM signal due to Δn and $\Delta\alpha$ is to measure the variation of the signal intensity with the crossing angle of the write beams, θ.[20] The angle at which the peak scattering efficiency occurs is sensitive to the relative magnitudes of the complex coupling constants which describe the interaction among the four laser beams in the crystal, D_1 and D_2. The real and imaginary parts of D_1 and D_2 were determined by using a Runge-Kutta technique to solve the four simultaneous differential equations describing the coupled waves in the crystal. The results were fitted to the data using a computer fitting routine and treating D_1^r, D_1^i, D_2^r, and D_2^i as adjustable parameters. The details

of this procedure are described fully in Ref. 20 and the values obtained for the coupling parameters are listed in Table III.

The relationships between the coupling parameters and the physical quantities of interest have been derived by analyzing the interaction of the laser beams with the ensemble of atoms.[24,25] The values of $\Delta\alpha$, Δn, and T_2 are given by

$$\Delta\alpha = -2\alpha D_2^i / D_1^i \ , \tag{11}$$

$$\Delta n = (\alpha c/\omega)(D_2^r / D_1^i) \ , \tag{12}$$

$$T_2 = (2\omega/c)(\Delta n/\Delta\alpha)(\omega - \omega_{21})^{-1} \ , \tag{13}$$

where α is the absorption coefficient for the write-beam wavelength ($\alpha = 5.57$ cm^{-1} at 588 nm), c is the speed of light, ω is the circular frequency of the write beams, and ω_{21} is the resonant frequency of the atomic transitions. The dephasing time can be separated into two contributions,

$$T_2^{-1} = (2T_1)^{-1} + \gamma \ , \tag{14}$$

where γ is the pure dephasing rate due to phonon scattering and T_1^{-1} represents the dephasing due to population relaxation. The values obtained for these parameters are listed in Table III. Using the value obtained for $\Delta\alpha$ in Eq. (10). A value for the excited-state absorption cross section can be obtained. The magnitude of σ_2 obtained in this way agrees with the value of 2.79×10^{-20} cm^2 reported from direct excited-state absorption measurements.[26]

The FWM signal-decay kinetics were found to be nonexponential and dependent on the crossing angle of the write beams for all temperatures for which a signal was visible. Above 160 K no FWM signal was observed,

TABLE III. Results of the four-wave mixing measurements in emerald with 3 at. % Cr^{3+} at 12 K.

Results from scattering-efficiency measurements	
D_2^r	2.0×10^{-6}
D_2^i	8.0×10^{-9}
D_1^r	5.0×10^{-7}
D_1^i	4.0×10^{-7}
$\Delta\alpha$	0.22 cm^{-1}
Δn	1.3×10^{-4}
T_2	1.2×10^{-12} s
η (absolute value for $\theta = 5.3°$)	4.0×10^{-3}
σ_2	2.8×10^{-20} cm^2
Results from grating-decay-kinetics measurements	
V	1.91×10^{5} s^{-1}
α'	2.55×10^{3} s^{-1}
D_r	2.79×10^{-7} cm^2/s
L_m	1.05×10^{-5} cm
L_D	3.06×10^{-5} cm
N_s	106

and this can be attributed to the small value of the fluorescence lifetime at these temperatures.[27] The signal kinetics are consistent with the predictions of the theory of Kenkre,[28] which describes the decay of a laser-induced grating in the presence of long-mean-free-path exciton migration. Again, it should be emphasized that the term exciton in this case refers to a Frenkel exciton in which the excitation energy is localized on an individual Cr^{3+} ion and can migrate on a lattice of Cr^{3+} ions. In the Kenkre model, the time dependence of the normalized FWM signal is given by

$$I_s(t) = e^{-2t/\tau}\left[J_0(bt)e^{-\alpha' t} + \alpha' \int_0^\infty du\, e^{-\alpha'(t-u)} J_0(b(t^2-u^2)^{1/2})\right]^2 , \tag{15}$$

where τ is the fluorescence lifetime, α' is the exciton scattering rate, and b is given by

$$b = \pi^2 a n V \theta / 45\lambda \ . \tag{16}$$

Here, V is the ion-ion–interaction rate, n is the index of refraction of the crystal, θ is the crossing angle of the write beams, and λ is the wavelength of the write beams. The average distance between uniformly distributed chromium ions in this sample is estimated to be $a = 9.87$ Å.

The FWM signal-decay kinetics were fitted using Eq. (15), treating α' and b as adjustable parameters. In order to emphasize the effects of energy migration, both the experimental data and the theoretical expression were divided by $\exp(-2t/\tau)$, which eliminates the fluorescence-decay contribution to the signal kinetics. A typical theoretical fit to the data is shown in Fig. 11. The excellent fit to the nonexponential shape of the curve indicates the presence of long-mean-free-path exciton migration. The values of α' and V obtained in this way can be used to calculate the parameters for characterizing the dynamics of the excitation migration. These include the resonant diffusion coefficient, the mean free path, the diffusion length, and the number of sites visited between scattering events,

$$D_r = 2V^2 a^2 / \alpha' \ , \tag{17}$$

$$L_m = 1.414 V_a / \alpha' \ , \tag{18}$$

$$L_D = (2D_r\tau)^{1/2} \ , \tag{19}$$

$$N_s = L_m / a \ . \tag{20}$$

The values of α', V, D_r, L_m, L_D, and N_s were calculated for each temperature and the values obtained at low temperature are listed in Table III. It should be pointed out that the expressions in Eqs. (17)–(20) are for migration on a uniform lattice and thus should be considered as approximate values for the random lattice associated with the case of interest here.

Figure 12 shows the temperature dependences of the

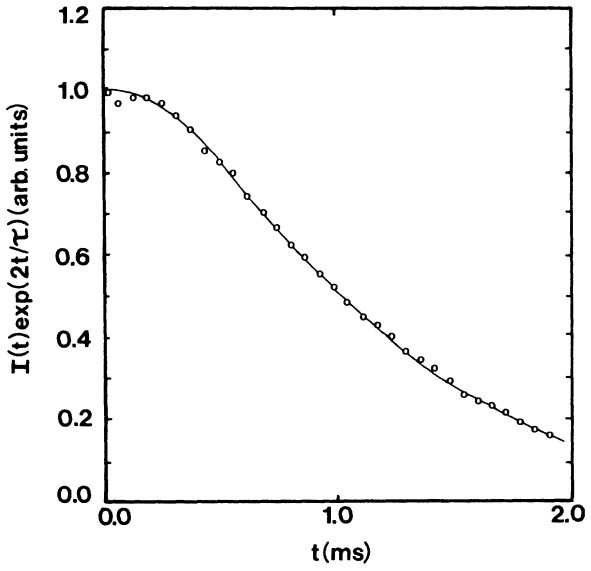

FIG. 11. Four-wave mixing decay kinetics (points) and theoretical fit to the data using Eq. (15) (solid line) after dividing by the fluorescence-decay factor. $T=16$ K and the crossing angle of the write beams is $\theta=20°$.

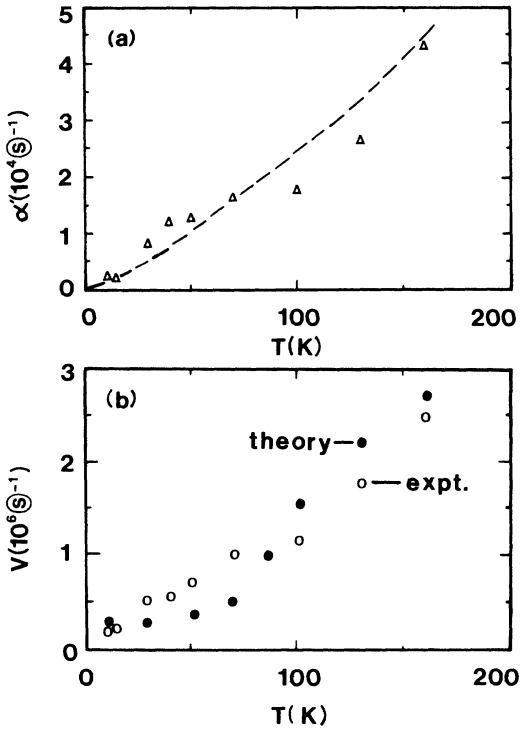

FIG. 12. Temperature dependence of (a) the ion-ion-interaction rate V and, (b) the exciton scattering rate α' obtained from FWM data. The dashed line in (a) and the solid points in (b) represent theoretical predictions.

ion-ion-interaction rate and the scattering rate. Both α' and V increase with temperature in this range. The increase in the former can be attributed to increased scattering by acoustic phonons. The theoretical treatment of Frenkel exciton scattering by acoustic phonons has been developed by Agranovich and co-workers.[29] The results of their work show that the scattering rate should increase as $T^{3/2}$ and the dashed line in Fig. 12(a) shows this type of variation. This provides a reasonable explanation for the experimentally observed temperature dependence of α'.

The temperature dependence of V can be attributed to the relative increase in the vibronic sideband emission compared to the R-line emission as temperature is raised. This causes an increase in the overlap between the emission and absorption spectra and an increase in the total emission rate. Both of these factors cause the ion-ion-interaction rate to increase. This can be approximated by

$$V(T)=C\tau^{-1}(I_{\text{vib}}/I_R)\ , \tag{21}$$

where the I's represent the intensities of the two components of the fluorescence spectrum and C is a proportionality constant. Using the values of the relative intensities and the fluorescence lifetime measured experimentally in Eq. (21) gives the theoretical points shown in Fig. 12(b), which are in good agreement with the experimentally determined temperature dependence for V.

Using Eq. (17), the diffusion coefficient for long-range resonant exciton migration can be determined. Figure 13 shows the results obtained using the experimental points for V and α'. The solid line in the figure is obtained using the theoretical curves given in Figs. 12(a) and 12(b). There is a good agreement between the two results.

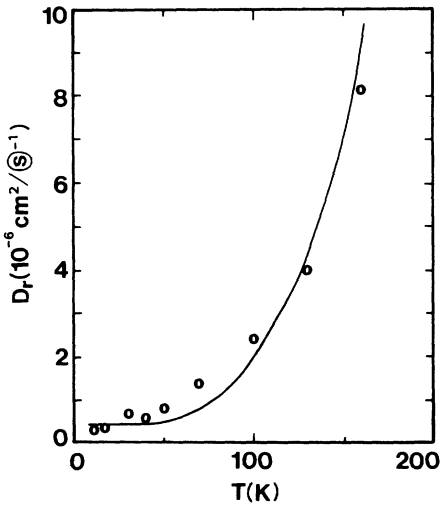

FIG. 13. Temperature dependence of the exciton diffusion coefficient obtained from FWM data. The solid line represents the theoretical prediction for D_r.

V. SUMMARY AND CONCLUSIONS

Laser site-selection spectroscopy shows that the Cr^{3+} ions in emerald have different types of local crystal-field environments. The origin of these different environments cannot be determined from available spectroscopic information. The beryl host structure does not have distinctly different lattice sites for the Al^{3+} ions for which the Cr^{3+} ions substitute. However, this type of spectral structure has been observed for many types of optically active ions in crystals and is generally attributed to two possible sources. The first is microscopic strains associated with neighboring lattice imperfections (either point defects or dislocations). The second is exchange interaction between pairs of Cr^{3+} ions. The identification of the origin of the spectral structure in emerald requires further work with a variety of samples having different concentrations of defects and of Cr^{3+} ions. However, it is not necessary to know the exact nature of the inequivalent environments to analyze the general dynamics of the energy-transfer processes in the material, which is the central interest of this work.

The results described here indicate that there are two different types of energy-transfer processes taking place in emerald. The first is short-range spectral migration among Cr^{3+} ions having different types of local crystal-field environments, while the second is long-range spatial migration among Cr^{3+} ions having resonant transition energies. The former evolves from ions having local environments leading to high-energy transitions in the spectral profile to ions having local environments leading to low-energy transitions. The relative concentration of the latter type of ions is about 2 orders of magnitude greater than the former. In this case the spectral transfer is consistent with an electric-dipole–dipole interaction mechanism and is independent of temperature at low temperature. The latter type of spatial transfer involves a stronger interaction mechanism between ions in the more concentrated type of environment, and the transfer rate increases with increasing temperature due to the increasing importance of vibronic emission.

For both types of energy transfer observed in this work, the multistep migration of energy is modeled as a mobile Frenkel exciton with excitation energy localized on an individual Cr^{3+} ion. Theoretical estimates can be made for the diffusion coefficient describing this type of process. For incoherent hopping migration via dipole-dipole interaction, the diffusion can be expressed as[30,31]

$$D_n=(4\pi N_i R_0^6/6\tau_i)\int_a^\infty R^{-2}\exp(-4\pi N_i R^3/3)dR \ . \tag{22}$$

Here, N_i is the concentration of ions in the type of site transferring the energy and τ_s is the fluorescence decay time of these ions. R_0 is the critical interaction distance which can be determined from the overlap of the emission and absorption spectra of the ions between which transfer is occurring. The lower limit of the integral is taken to be the nearest-neighbor distance of 4.6 Å. The value of D_n calculated from this expression using measured spectral data is listed in Table II. The result is the same order of magnitude as that determined from the experimental results described above. This is also consistent with the values obtained for the diffusion coefficient in other materials measured under similar conditions.

The order of magnitude of the diffusion coefficient describing long-range resonant energy migration is significantly larger than the spectral diffusion coefficient. If Eq. (22) is solved using the greater concentration of ions in sites *c*, *d*, and *e*, a value is predicted for the diffusion coefficient of the order of 4×10^{10} cm^2s^{-1}, which is still much smaller than the diffusion coefficient determined by FWM results. The only way the higher values of the diffusion coefficient to be predicted theoretically is to assume a stronger mechanism of the ion-ion interaction. If the energy transfer takes place by exchange interaction, Eq. (22) is replaced by[32]

$$D_{ex}=(2\pi N_i P_o/3)\int_0^\infty R^4\exp[-(2R/L+4\pi N_i R^3/3)] \ , \tag{23}$$

where L is the average Bohr radius of the electron wave functions and P_o is a constant that depends on the spatial overlap of the wave functions and the spectral overlap integral. These parameters have not been determined specifically for emerald, and thus an exact value for D_{ex} cannot be obtained for this system. However, for Cr^{3+} ions in Al_2O_3 (ruby) these parameters have been found to be[11,33] $L=0.97$ Å and $P_o=4.3\times10^{14}$ s^{-1}. Using these values in Eq. (23) gives $D_{ex}\approx10^{-7}$ cm^2s^{-1}, which is in good agreement with the value of D_r obtained from FWM measurements. The value of L will always be close to 1 Å, but P_o can vary appreciably from host to host. The nearest-neighbor spacings between Cr^{3+} ions in the ruby lattice are smaller than in emerald, but the concentration of Cr^{3+} ions present in our emerald sample is much greater than in most ruby samples.[11,33] Thus the predicted value of D_{ex} obtained from Eq. (23) must be taken as only a rough estimate for emerald. However, the point of this analysis is to show that a strong, short-range interaction mechanism such as exchange can lead to a diffusion coefficient of the order of magnitude of that obtained from FWM measurements.

It should be emphasized that there is no discrepancy between the results of TRSSS and FWM measurements. The former probes the properties of energy transfer from ions in a specific type environment to ions in other types of environments. These results are strongly affected by the fact that the concentration of ions in activator environments is significantly greater than the concentration of ions in sensitizer environments. This leads to a dipole-dipole interaction with negligible backtransfer. On the other hand, the FWM measurements are only sensitive to energy migration of distances of the order of a grating spacing. Thus the energy transfer measured by this method takes place among the ions in the highest-concentration environment through a strong interaction mechanism such as exchange. Both types of measurements are necessary to obtain a complete picture of the different types of energy-transfer processes taking place in the sample.

The value obtained for D_r is similar to that obtained

for alexandrite.[20] However, the temperature dependence of D_r is quite different in alexandrite and emerald. In both materials the scattering rate limiting the mean free path of the excitons was found to increase with temperature. However, at low temperatures the ion-ion–interaction rate in alexandrite is independent of temperature, whereas in emerald it increases with temperature. This is because the vibronic emission transitions begin to become important at much lower temperatures in emerald than in alexandrite, as can be seen from their fluorescence spectra. This is associated with the weaker crystal field at the site of the Cr^{3+} ion in the emerald host compared to alexandrite.

The dephasing time found for emerald is less than the values found from ruby and alexandrite.[20] This follows a trend of decreasing T_2 with decreasing crystal-field strength. Assuming the dephasing is dominated by the radiationless relaxation to the bottom of the ^2E potential well, the dependence on crystal-field strength implies direct relaxation in the ^2E level instead of initial relaxation in the $^4T_2$ level. Since the two states are mixed, the branching ratio for radiationless relaxation will be determined by the relative densities of states at the terminal point of the absorption transition. For the materials investigated thus far, the branching ratio in the ^2E level will be much greater than that in the $^4T_2$ level. For hosts with smaller crystal-field strengths the relative magnitudes of these branching ratios will be quite different. Therefore, making similar measurements on low-crystal-field-strength materials is an important test of this model for interpreting the T_2 results.

ACKNOWLEDGMENTS

The Oklahoma State University part of this work was sponsored by the U.S. Army Research Office. One of us (G.J.Q.) was supported by a grant provided by the U.S. Air Force Weapons Laboratory.

*Present address: Naval Research Laboratories, Code 6551, Washington, D.C. 20375-5000.

†Permanent address: Institute of Physics, Polish Academy of Sciences, Aleja Lotnikow 32/46, 02-668, Warsaw, Poland.

[1]M. L. Shand, in *Proceedings of the International Conference on Lasers '82,* edited by R. C. Powell (SPS Press, McLean, VA, 1982), p. 799.

[2]J. Buchert, A. Katz, and R. R. Alfano, in *Proceedings of the International Conference on Lasers '82,* Ref. 1, p. 791.

[3]S. Lai, J. Opt. Soc. Am. B **4**, 1286 (1987).

[4]D. L. Wood, J. Chem. Phys. **42**, 3404 (1965).

[5]S. V. Brum-Grzhimailo and G. V. Klimusheva, Opt. Spektrosk. **8**, 3421 (1960) [Opt. Spectrosc. (USSR) **8**, 179 (1960)].

[6]B. Morosin, Acta Cryrstallogr. Sect. B **28**, 1899 (1972).

[7]B. Halperin, D. Nicollin, and J. A. Koningstein, Chem. Phys. **42**, 277 (1979).

[8]T. F. Veremeichik, Phys. Status Solidi B **124**, 719 (1984).

[9]Z. Hasan, S. T. Keany, and N. B. Manson, J. Phys. C **19**, 6381 (1986).

[10]A. Edgar and D. R. Hutton, J. Phys. C **11**, 5051 (1978).

[11]W. L. Bragg and J. West, Proc. R. Soc. London, Ser. A **111**, 691 (1926).

[12]R. J. Birgeneau, J. Chem. Phys. **50**, 4282 (1969).

[13]R. G. Wyckoff, *Crystal Structure* (Interscience, New York, 1948), Vol. II, p. 7.

[14]E. F. Farrell, J. H. Fang, and R. E. Newnham, Amer. Mineral. **48**, 805 (1963).

[15]D. L. Wood, J. Ferguson, K. Knox, and J. F. Dillon, Jr., J. Chem. Phys. **37**, 890 (1963).

[16]P. Kisliuk and C. A. Moore, Phys. Rev. **160**, 307 (1967).

[17]W. H. Fonger and C. W. Struck, Phys. Rev. B **11**, 3251 (1975).

[18]D. Sardar and R. C. Powell, J. Lumin. **22**, 349 (1981).

[19]H. C. Chow and R. C. Powell, Phys. Rev. B **21**, 3785 (1980).

[20]A. Suchocki, G. D. Gilliland, and R. C. Powell, Phys. Rev. B **35**, 5830 (1987).

[21]H. Kogelnik, Bell Syst. Tech. J. **48**, 2909 (1969).

[22]K. O. Hill, Appl. Opt. **10**, 1695 (1971).

[23]A. M. Ghazzawi, J. K. Tyminski, R. C. Powell, and J. C. Walling, Phys. Rev. B **30**, 7182 (1984).

[24]A. Yariv and D. M. Pepper, Opt. Lett. **1**, 16 (1977).

[25]R. L. Abrams and R. C. Lind, Opt. Lett. **2**, 94 (1978); **3**, 205 (1978).

[26]W. M. Fairbank, Jr., G. K. Klauminzer, and A. L. Schawlow, Phys. Rev. B **11**, 60 (1976).

[27]A. Suchocki, J. D. Allen, R. C. Powell, and G. M. Loiocono, Phys. Rev. B **36**, 6729 (1987).

[28]Y. M. Wong and V. M. Kenkre, Phys. Rev. B **22**, 3072 (1980); V. M. Kenkre and D. Schmid, *ibid.* **31**, 2430 (1985).

[29]V. M. Agranovich and M. D. Galanin, *Electronic Excitation Energy Transfer in Condensed Matter* (North-Holland, Amsterdam, 1982); V. M. Agranovich and Yu. V. Konobeev, Opt. Spektrosk. **6**, 642 (1959); **6**, 648 (1959) [Opt. Spectrosc. (USSR) **6**, 155 (1959); **6**, 421 (1959)]; Phys. Status Solidi **27**, 435 (1968).

[30]S. Chandraskhar, Rev. Mod. Phys. **15**, 1 (1943).

[31]T. Forster, Ann. Phys. (Leipzig) **2**, 55 (1948); Z. Naturforsch. **49**, 321 (1949).

[32]D. L. Dexter, J. Chem. Phys. **22**, 836 (1953).

[33]G. F. Imbusch, Phys. Rev. **153**, 326 (1967).